Signal Processing 128 (2016) 459–473

Contents lists available at ScienceDirect

Signal Processing

journal homepage: www.elsevier.com/locate/sigpro

# A study on image denoising in contourlet domain using the alpha-stable family of distributions

H. Sadreazami, M. Omair Ahmad *, M.N.S. Swamy

*Center for Signal Processing and Communications, Department of Electrical and Computer Engineering, Concordia University, Montreal, QC, Canada H3G 1M8*

ARTICLE INFO

*Article history:*
Received 9 July 2015
Received in revised form
16 February 2016
Accepted 18 May 2016
Available online 21 May 2016

*Keywords:*
Image denoising
Contourlet transform
Alpha-stable distribution
Bayesian MAP estimator
Bayesian MMAE estimator

ABSTRACT

In the past decade, several image denoising techniques have been developed aiming at recovering signals from noisy data as much as possible along with preserving the features of an image. This paper proposes a new image denoising method in the contourlet domain by using the alpha-stable family of distributions as a prior for contourlet image coefficients. The univariate symmetric alpha-stable distribution (S$\alpha$S) is mostly suited for modeling of the i.i.d. contourlet coefficients with high non-Gaussian property and heavy tails. In addition, the bivariate S$\alpha$S exploits the dependencies between the coefficients across scales. In this paper, using the univariate and bivariate priors, Bayesian minimum mean absolute error and maximum a posteriori estimators are developed in order to estimate the noise-free contourlet coefficients. To estimate the parameters of the alpha-stable distribution, a spatially-adaptive method using fractional lower order moments is proposed. It is shown that the proposed parameter estimation method is superior to the maximum likelihood method. An extension to color image denoising is also developed. Experiments are carried out using noise-free images corrupted by additive Gaussian noise, and the results show that the proposed denoising method outperforms other existing methods in terms of the peak signal-to-noise ratio and mean structural similarity index, as well as in visual quality of the denoised images.



## 1. Introduction

Denoising is a problem of estimating the noise-free image from noisy observations while preserving the image features. The image denoising techniques may be classified into spatial [1,2], and transform domain [3–7] approaches. The image denoising in the transform domain has attracted considerable interest in view of its improved performance at recovering signals from noisy data. In the transform domain approach, denoising process is performed on the transformed coefficients of different transforms such as wavelet transform [5,6]. In fact, the wavelet shrinkage method, proposed by Donoho [7], is the most demonstrative one in which a simple and non-probabilistic thresholding is used to remove noise from an image. However, it is known that the wavelet transform is good at isolating discontinuities at edge points and cannot efficiently capture the smoothness along the contour [8,9]. In addition, applying wavelet to an image results in capturing limited directional information. In [10], the principal component analysis has been proposed to overcome the drawbacks of the wavelet transform in highly-structured images. However, these components are highly affected by the noise. In [11], the K-SVD algorithm has been proposed for the same purpose. However, exhaustive search in learned dictionaries gives rise to a time-consuming algorithm. Another class of image denoising techniques is the non-local means (NLM) algorithms [12–18]. The NLM algorithms estimate a pixel by a weighted average of the local and non-local pixels throughout the image and perform denoising by exploiting the natural redundancy of the patterns inside an image. In [19], similar to motion estimation algorithms, a block-wise matching has been used to preprocess the noisy image followed by a transform domain shrinkage, known as BM3D. However, the accuracy of such block correlations is highly dependent on the noise. In [20], a patch-based locally-optimal Wiener filter has been proposed for image denoising. This method uses similar patches to estimate the filter parameters. In [21], a spatially adaptive iterative singular-value thresholding method has been proposed, which provides slightly better performance in terms of peak signal-to-noise ratio (PSNR) than that provided by BM3D.

To enhance the sparsity and effectively capture the directional information in natural images, other multi-scale and multi-resolutional transforms, such as wavelet-packets [22], complex wavelet [23–25], curvelet [26], or contourlet [8,9,27–29] transforms, have been proposed. The better sparseness and decorrelation properties of

* Corresponding author.
*E-mail address:* omair@ece.concordia.ca (M.O. Ahmad).

http://dx.doi.org/10.1016/j.sigpro.2016.05.018
0165-1684/

these transforms result in improved image denoising schemes. In [24,30], the image denoising is performed in complex wavelet domain, which provides more directionality than that provided by wavelet, yet is not efficient to handle 2-D singularities. In [26], the curvelet domain image denoising has been proposed. The curvelet transform provides higher directional information of an image resulting in a denoising scheme with visually improved image and more edge preservation. However, the curvelet transform has originally been defined on concentric circles in the continuous domain and the process of discretization is complex and time-consuming. Therefore, to overcome these disadvantages of the curvelet transform, the contourlet transform has been proposed in [9].

The contourlet transform provides not only the multiscale and time-frequency localization features of the wavelet transform, but also offers a higher degree of directionality with better sparseness. In view of this, it has been shown in [9] that image denoising in the contourlet domain is superior to that in the wavelet domain. Most of the image denoising algorithms in the contourlet domain have been developed based on the thresholding or shrinkage functions [9,27], in which the coefficients with small magnitudes are simply set to zero, while the rest are kept unchanged in the case of hard-thresholding, and shrunk in the case of soft-thresholding.

In recent years, statistical models have been adopted for the transform domain coefficients in which the image and noise are modeled as random fields and Bayesian methods are employed to develop shrinkage functions for estimation of the noise-free coefficients from the noisy observations. It is to be noted that the prior distributions for the original image and the noise have considerable effect on the performance of the denoising process. Several prior distributions have been employed to characterize the transform coefficient properties such as their sparsity, i.e., having a large number of small coefficients along with a small number of large coefficients [5,6,25,31–38]. The contourlet coefficients have been shown to be highly non-Gaussian [9,39–41], i.e., having large peaks around zero and tails heavier than that of a Gaussian probability density function (PDF). In view of this, the contourlet coefficients have been modeled formerly by the generalized Gaussian distribution [9].

Through modeling of the actual data, we have shown in [40,41], that the contourlet-domain subband decomposition of real images has significant non-Gaussian statistics that are best described by families of heavy-tailed distributions, such as the alpha-stable family. Motivated by the modeling results, in this work, we propose a new image denoising technique in the contourlet domain based on the alpha-stable family of distributions as a prior for the contourlet coefficients. We will derive the Bayesian minimum mean absolute error (MMAE) and maximum a posteriori (MAP) estimators using the alpha-stable distribution to obtain the noise-free contourlet coefficients. We first assume that the contourlet coefficients are independent and identically distributed by the univariate alpha-stable distribution. Then, we consider the across-scale dependencies of the contourlet coefficients by employing the bivariate alpha-stable distribution to capture these dependencies. In order to estimate the parameters of the model, we propose a spatially-adaptive method based on fractional lower order moments. An extension to color image denoising will also be developed. Several experiments are conducted to evaluate the performance of the proposed denoising scheme and to compare it with those of the current state-of-the-art techniques. The estimated images are compared with the original ones in terms of the PSNR and mean structural similarity (MSSIM) index, as well as in visual quality of the denoised images.

The paper is organized as follows: Section 2 presents briefly the contourlet transform. In Section 3, the alpha-stable distribution and results on modeling the contourlet coefficients of images using this distribution are presented. In Section 4, the image denoising algorithm based on either the MMAE or MAP estimator is presented. In Section 5, the performance of the proposed algorithms is examined and compared to those of the other existing methods. Section 6 concludes the paper.

## 2. The contourlet transform

The contourlet transform, a new image decomposition scheme proposed in [9], provides an efficient representation for two-dimensional signals with smooth contours and in this case, outperforms the wavelet transform, which fails to recognize the smoothness of the contour. The contourlet transform also has the multiscale and time-frequency localization features of the wavelet transform [42]. In addition, it offers a higher degree of directionality with better sparseness. Further, in view of the use of iterated filter banks, it is computationally efficient [9]. There are number of other structures, such as the complex wavelet [23], ridgelet [43,44] and curvelet [45,46], that also provide multiscale and directional image representation. However, most of these structures are not flexible in the sense that one cannot use different number of directions at each scale. Moreover, since the contourlet transform has been introduced in the discrete domain, it overcomes the blocking artifact deficiency of the curvelet transform (Fig. 1). It should be noted that the use of downsamplers and upsamplers in the structure of the contourlet transform makes it shift-variant, which may produce artifacts around the singularities, e.g., edges. Hence, the cycle spinning method [27,47] is employed to compensate for the lack of translation invariance. It is a simple, yet efficient, method to improve the denoising performance for a shift-variant transform. In fact, the cycle spinning is to average out the translation dependence of the subsampled contourlet transform and can be expressed as

$$\hat{I} = \frac{1}{M \times N} \sum_{m=1}^{M} \sum_{n=1}^{N} \left( ICT\left(S_{-m,-n}\left(h\left(CT\left(S_{m,n}(I)\right)\right)\right)\right) \right) \tag{1}$$

in which $I$ and $\hat{I}$ are noisy and denoised images, CT and ICT are the contourlet transform and its inverse, respectively, $S_{m,n}$ is the cycle spinning operator with $(m,n)$ as shifts in the horizontal and vertical directions, and $h$ is the denoising operator in the contourlet domain [47].

## 3. Modeling of contourlet coefficients using the alpha-stable distribution

In order to model the contourlet subband coefficients of an image, we propose the use of $S\alpha S$ distribution as a prior for the contourlet coefficients of a noisy image. A random variable $X \sim S_\alpha(\gamma, \beta, \delta)$ with univariate alpha-stable distribution is described by its characteristic function given by [48]

$$\Phi_{\alpha,\gamma,\beta,\delta}(\omega) = \exp\left\{ j\delta\omega - \gamma|\omega|^\alpha [1 + j\beta\, \mathrm{sign}(\omega) \varpi(\omega, \alpha)] \right\} \tag{2}$$

where

$$\varpi(\omega, \alpha) = \begin{cases} \tan \dfrac{\alpha\pi}{2} & \text{if } \alpha \neq 1 \\ \dfrac{2}{\pi} \log |\omega| & \text{if } \alpha = 1 \end{cases} \tag{3}$$

and $\alpha$ is a characteristic exponent, $(0 < \alpha \le 2)$, $\beta \in [-1, 1]$ is a skewness parameter, $\delta \in \Re$ is a location parameter and $\gamma > 0$ a dispersion parameter. For a particular class of the alpha-stable distributions, called the standard symmetric alpha-stable (S$\alpha$S) distribution, $\delta = \beta = 0$. The characteristic exponent $\alpha$ is the most important parameter in determining the shape of the distribution [48,49]. The smaller the value of $\alpha$, the heavier the tail of the distribution. This implies that random variables following the S$\alpha$S distribution with small characteristic exponents are highly impulsive. In

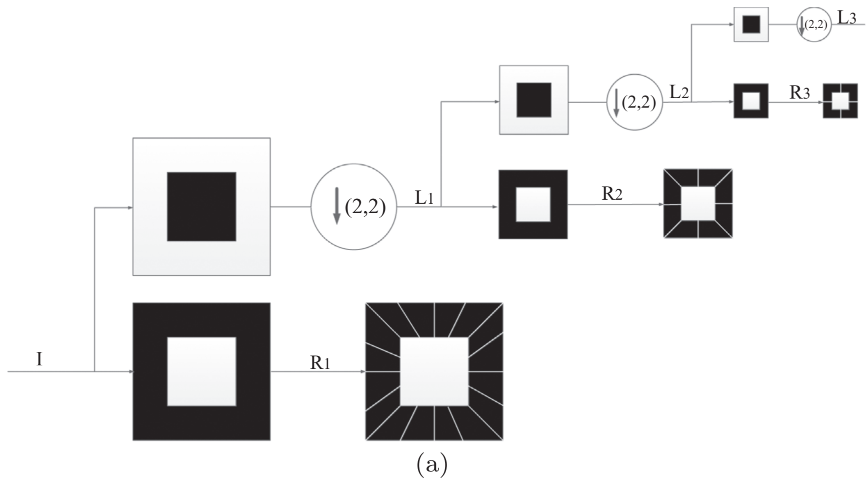


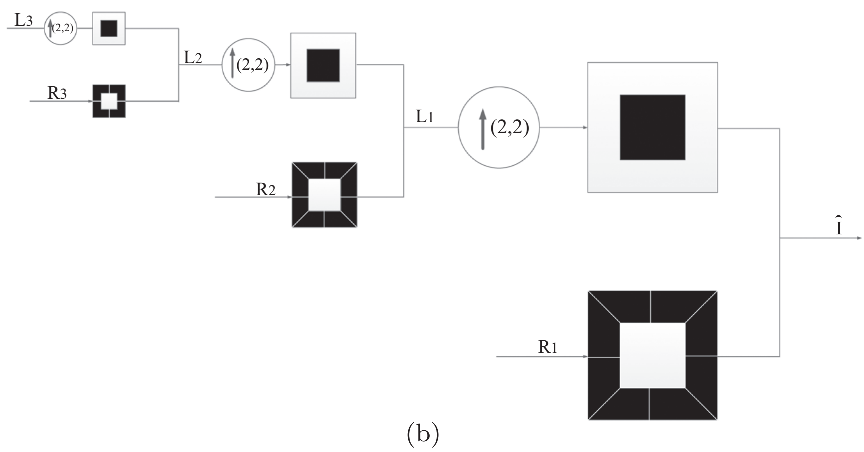


**Fig. 1.** Block diagram of the contourlet filter bank structure. (a) In analysis, the Laplacian pyramid is applied to the original image resulting in a coarse image, denoted by *L*, and a residual image, denoted by *R*. The residual image is fed into the directional filter bank to obtain directional information. (b) In synthesis, the original image is reconstructed using the same filters for the Laplacian pyramid as in analysis part.

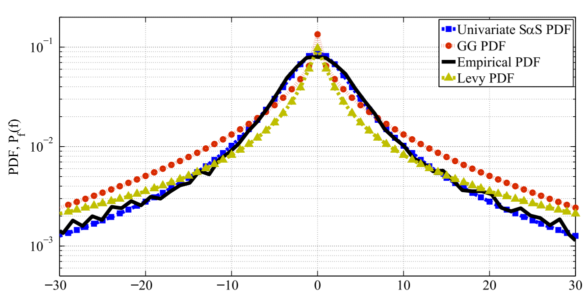


**Fig. 2.** PDF of the empirical data as well as that of the S$\alpha$S, Levy and GG distributions for the *Barbara* image in the finest subband.

order to model the contourlet subband coefficients of an image, we propose the use of S$\alpha$S distribution to satisfy the large peak and heavy-tail properties of these coefficients. We investigate as to how accurately the alpha-stable distribution fits the distribution of the contourlet coefficients. For this purpose, we examine the histograms of the actual data as well as that of the S$\alpha$S, Levy and generalized Gaussian PDFs for a number of test images. The modeling performance of the contourlet coefficients for one of the test images, *Barbara* image, is illustrated in Fig. 2. It is evident from this figure that the univariate S$\alpha$S distribution can fit the empirical data better than the generalized Gaussian and Levy distributions can. Similar results have also been obtained for other test images [41]. Moreover, to quantify the performance of the PDFs, we employ the Kolmogorov–Smirnov distance (KSD) given by $\max|\int P_f(f) - \hat{P}_f(f)df|$, in which $P_f(f)$ denotes the PDF of the random variable and $\hat{P}_f(f)$ represents the PDF of the empirical data. Table 1 gives the values of the KSD metric for the S$\alpha$S, Cauchy, GG, Laplacian and Levy PDFs of the image contourlet coefficients in the two finest scales averaged over the subset

**Table 1**
KSD values of the S$\alpha$S, Cauchy, GG, Laplacian and Levy distributions in the modeling of contourlet coefficients averaged over a set of 10,000 images taken from the dataset in [50], $S_{ij}$ denoting the subband in scale *i* and direction *j*.

| Direction | KSD | | | | |
|---|---|---|---|---|---|
| | S$\alpha$S | Cauchy | GG | Laplacian | Levy |
| $S_{21}$ | 0.1014 | 0.1044 | 0.1321 | 0.1234 | 0.1206 |
| $S_{22}$ | 0.1083 | 0.1097 | 0.1436 | 0.1297 | 0.1229 |
| $S_{23}$ | 0.1156 | 0.1204 | 0.1432 | 0.1357 | 0.1349 |
| $S_{24}$ | 0.0880 | 0.0923 | 0.1269 | 0.1224 | 0.1189 |
| $S_{25}$ | 0.1253 | 0.1275 | 0.1355 | 0.1291 | 0.1215 |
| $S_{26}$ | 0.1189 | 0.1229 | 0.1347 | 0.1305 | 0.1279 |
| $S_{27}$ | 0.0798 | 0.0822 | 0.1351 | 0.1403 | 0.1381 |
| $S_{28}$ | 0.0819 | 0.0835 | 0.1281 | 0.1280 | 0.1253 |
| $S_{11}$ | 0.1135 | 0.1302 | 0.1347 | 0.1468 | 0.1361 |
| $S_{12}$ | 0.0875 | 0.0881 | 0.0895 | 0.1030 | 0.1049 |
| $S_{13}$ | 0.0958 | 0.0959 | 0.0984 | 0.1117 | 0.1012 |
| $S_{14}$ | 0.0727 | 0.0734 | 0.0759 | 0.0995 | 0.0853 |
| $S_{15}$ | 0.0917 | 0.0949 | 0.0928 | 0.1073 | 0.0947 |
| $S_{16}$ | 0.0956 | 0.0957 | 0.0982 | 0.1090 | 0.0979 |
| $S_{17}$ | 0.0884 | 0.0889 | 0.0885 | 0.1063 | 0.0914 |
| $S_{18}$ | 0.0900 | 0.0904 | 0.0878 | 0.1098 | 0.0919 |

of 10,000 images taken from the dataset in [50]. It is seen from this table that the univariate S$\alpha$S distribution provides a better fit to the empirical data than the Cauchy, GG, Laplacian and Levy distributions

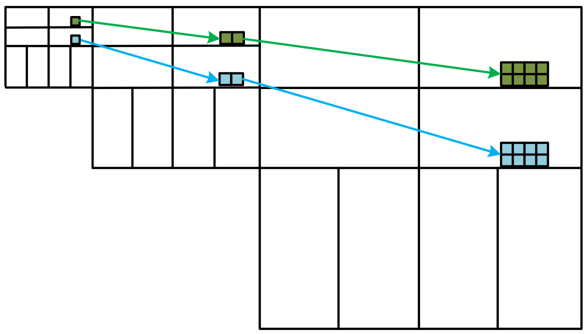

**Fig. 3.** Parent–children relationship for a three-scale contourlet decomposition with eight directions in each scale.

do.

It is known that the contourlet coefficients of images have across-scale dependencies [39]. Fig. 3 depicts a parent–children relationship for a three-scale contourlet decomposition with eight directions in each scale. These dependencies play an important role in the modeling of the contourlet coefficients. In addition, the contourlet coefficients are non-Gaussian [10,40], i.e., have large peaks around zero and tails heavier than that of a Gaussian PDF. In view of this, we also model the contourlet coefficients of an image using the bivariate alpha-stable distribution in order to not only capture the heavy tails of the distribution of the contourlet coefficients, but also to take into account the contourlet coefficient dependencies across scales. The standard bivariate S$\alpha$S is characterized by its characteristic function as

$$\Phi_{\alpha,\gamma}(\omega_1, \omega_2) = \exp\left(-\gamma\left(\sqrt{\omega_1^2 + \omega_2^2}\right)^{\alpha}\right) \tag{4}$$

Fig. 4 shows the distribution of the coefficients conditioned on its parent value in the four directional subbands of the finest scale for one of the test images, *Barbara* image. It is seen from this figure that the

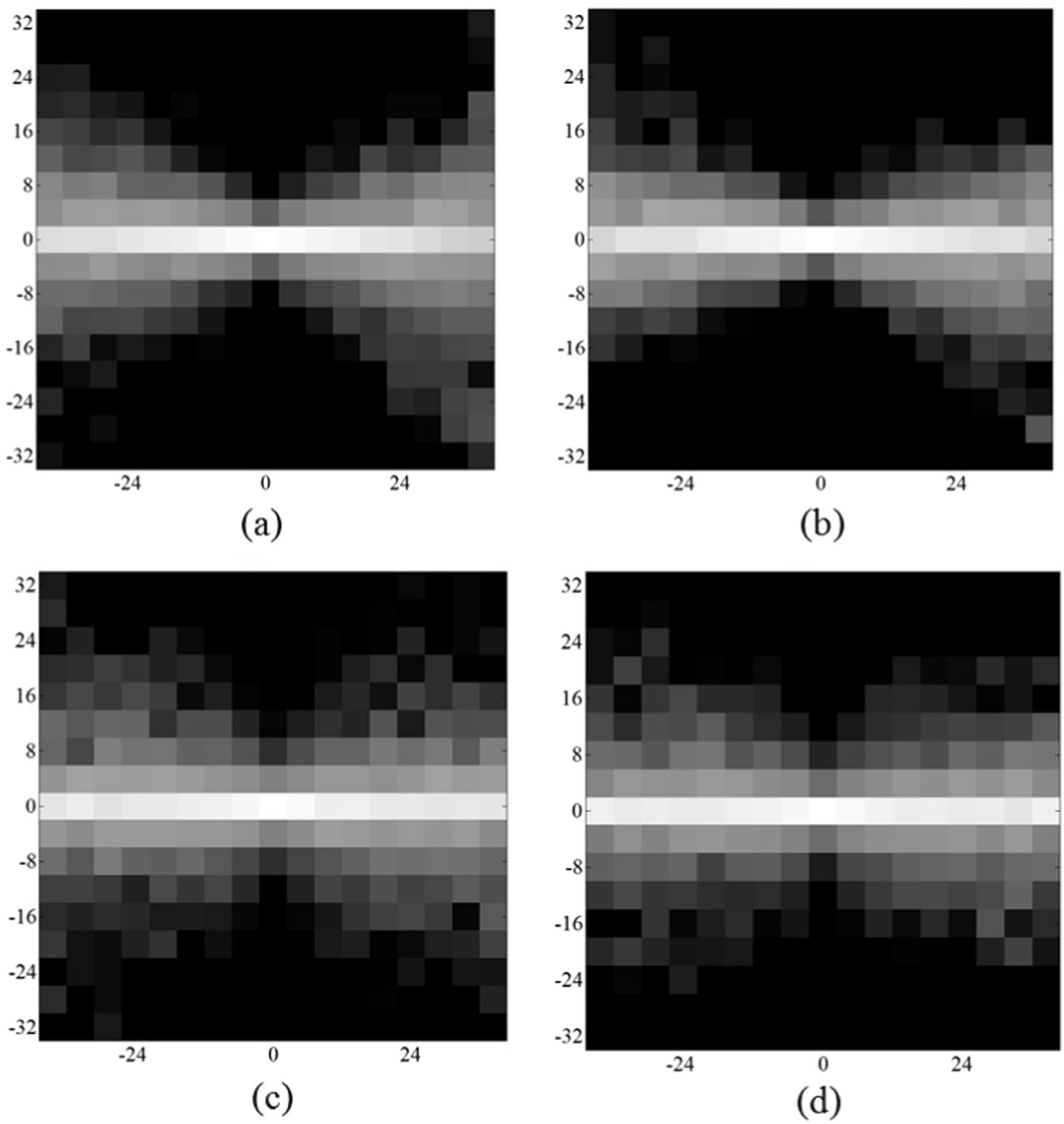


**Fig. 4.** Distribution of the contourlet coefficients (vertical axis) conditioned on the corresponding coarser-scale coefficient, i.e., parent coefficient (horizontal axis), in the four directional subbands of the *Barbara* image; a normalized pair of parent and child coefficients is considered.

conditional histograms for various directional subbands resemble a bow-tie shape indicating the dependency between the children and their parents. Fig. 5 shows the joint histogram of the contourlet coefficients across scales for the *Barbara* image along with the corresponding bivariate S$\alpha$S PDF. It can be seen from this figure that the bivariate S$\alpha$S PDF can suitably model the parent–children relationship of the contourlet coefficients across two consecutive scales.

## 4. Proposed denoising algorithm

Let a noise-free image $X$ be contaminated by an independent, additive white Gaussian noise $N$ with a zero-valued mean and known standard deviation $\sigma_\eta$. The corresponding noisy image $Y$ is then given by

$$Y = X + N \tag{5}$$

Contourlet transform is now applied to the noisy image. Let $Y$ be decomposed into $j = 1, \ldots, J$ scales and $d = 1, \ldots, D$ direction subbands by the contourlet transform. We then have

$$y_j^d(m, n) = x_j^d(m, n) + \eta_j^d(m, n) \tag{6}$$

where $y_j^d(m, n)$, $x_j^d(m, n)$ and $\eta_j^d(m, n)$ denote the $(m,n)$th contourlet coefficient of the noisy image at scale $j$ with direction $d$, the noise-free coefficient and the corresponding noise component, respectively. It should be noted that the noise remains Gaussian after applying the contourlet transform. For notational simplicity, we drop the subscripts and indices as well, and henceforth use $y$, $x$ and $\eta$ throughout the paper.

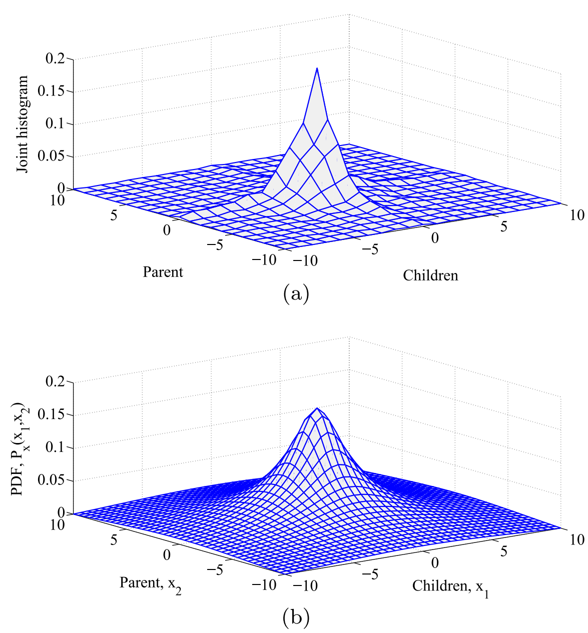


**Fig. 5.** (a) Empirical joint child–parent histogram across two scales of the contourlet coefficients in the fourth direction for the *Barbara* image. (b) The corresponding bivariate S$\alpha$S distribution.

### 4.1. Bayesian MAP estimator for Gaussian noise

The Bayesian method imposes a prior model on the contourlet coefficients that describe their distribution. In this work, we propose the S$\alpha$S distribution as a prior for modeling the contourlet coefficients $x$ corresponding to a specific subband of a noise-free image. We assume that the probabilistic model associated with the noisy data $y$ conditioned on $x$ is Gaussian:

$$y|x \sim N(x, \mu = 0, \sigma_\eta^2) \tag{7}$$

The noise distribution can be expressed as $P_\eta(y - x) = \frac{1}{\sqrt{2\pi}\sigma_\eta}\exp\left\{-\frac{(y-x)^2}{2\sigma_\eta^2}\right\}$. For estimating the original image, i.e., the noise-free coefficients $x$, given the noisy observation $y$, we employ the MAP estimator. Using the Bayes rule, the MAP estimator is defined by

$$\begin{aligned}\hat{x}(y) &\propto \arg\ \max P_{x|y}(x|y)\\ &\propto \arg\ \max P_{y|x}(y|x)P_x(x)\\ &\propto \arg\ \max P_\eta(y - x)P_x(x)\end{aligned} \tag{8}$$

where $P_x(x)$ is the PDF of the contourlet coefficients of the noise-free image. To obtain the MAP estimate, after inserting $P_\eta(\eta)$ into (8), the derivative of the logarithm of the argument in (8) is set to zero resulting in

$$\frac{\hat{x} - y}{\sigma_\eta^2} + \frac{\partial}{\partial y}(-\ln(P_x(y))) = 0 \tag{9}$$

We now need a model for the distribution of the contourlet coefficients $P_x(x)$. At this stage, we consider the following three cases.

*Case* 1: $P_x(x) \sim N(0, \sigma^2)$, where $\alpha = 2$ and $\sigma^2$ is the variance of the Gaussian PDF.
*Case* 2: $P_x(x) = \frac{\gamma}{\pi(x^2+\gamma^2)}$, where $\alpha = 1$ and $\gamma$ is the dispersion parameter of the Cauchy PDF.
*Case* 3: $P_x(x) = \sqrt{\frac{\gamma}{2\pi}}\frac{e^{\frac{-\gamma}{2x}}}{x^{\frac{3}{2}}}$, where $\alpha = 0.5$ and $\gamma$ is the dispersion parameter of the Levy PDF.
*Case* 4: Best-fit S$\alpha$S for which there is no closed-form PDF.

It may be noted that Cases 1 to 3 above are the special cases of the alpha-stable PDF having closed-form expressions [48]. For case 1, the estimate $\hat{x}$ for the Gaussian data is obtained from (9) as

$$\hat{x}_i(y) = \frac{\sigma_x^2}{\sigma_x^2 + \sigma_\eta^2}y \tag{10}$$

which is the minimum mean square error (MMSE) solution for the Bayesian estimator. For Cases 2–4, the Bayesian MAP estimator for non-Gaussian data is obtained from (9) as

$$\hat{x}(y) = \mathrm{sign}(y)(|y| - \sigma_\eta^2|M|)_+ \tag{11}$$

where $M = \frac{\partial \ln P_Y(y)}{\partial y}$ and $(z)_+ = \max(z, 0)$. It may be mentioned that

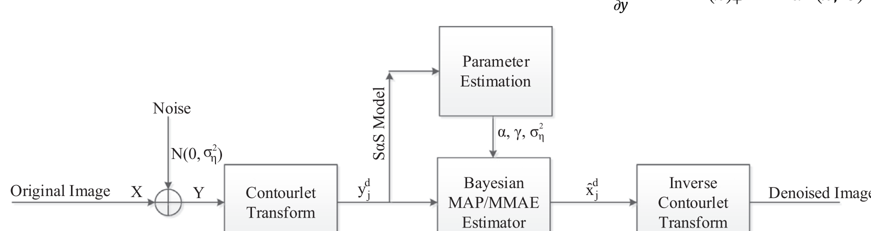


**Fig. 6.** Block diagram of the proposed denoising algorithm.

**Table 2**
PSNR values obtained using denoising methods employing the alpha-stable family of distributions in wavelet (WT) and contourlet (CT) domains. (Best result shown in bold.)

| $\sigma_\eta$/PSNR | Cauchy | | SαS-MAP | | SαS-MMAE | | Bi-SαS-MAP | | Bi-SαS-MMAE | |
|---|---|---|---|---|---|---|---|---|---|---|
| | WT | CT | WT | CT | WT | CT | WT | CT | WT | CT |
| Barbara | | | | | | | | | | |
| 10/28.13 | 32.22 | 32.71 | 32.60 | 32.97 | 32.78 | 33.62 | 33.34 | 34.61 | 33.70 | **34.89** |
| 15/24.61 | 30.41 | 30.66 | 30.46 | 31.01 | 30.77 | 31.34 | 31.17 | 32.86 | 31.42 | **33.03** |
| 20/22.13 | 28.42 | 28.74 | 28.56 | 29.21 | 28.97 | 29.47 | 29.22 | 31.19 | 29.77 | **31.65** |
| 25/20.17 | 26.87 | 26.99 | 26.31 | 28.09 | 27.10 | 28.53 | 28.22 | 30.23 | 28.76 | **30.61** |
| 30/18.63 | 24.61 | 25.16 | 24.93 | 26.23 | 25.39 | 26.74 | 26.51 | 27.84 | 26.98 | **28.24** |
| 40/16.14 | 22.64 | 22.97 | 22.74 | 24.03 | 23.11 | 24.95 | 24.83 | 26.58 | 25.74 | **26.97** |
| Peppers | | | | | | | | | | |
| 10/28.13 | 32.13 | 32.45 | 32.31 | 32.65 | 32.60 | 33.41 | 33.02 | 34.29 | 33.41 | **34.59** |
| 15/24.61 | 30.05 | 30.35 | 30.21 | 30.80 | 30.62 | 31.13 | 30.89 | 32.55 | 31.06 | **32.73** |
| 20/22.15 | 28.24 | 28.33 | 28.25 | 29.10 | 28.76 | 29.34 | 29.14 | 30.51 | 29.51 | **30.87** |
| 25/20.17 | 26.56 | 26.79 | 26.74 | 27.92 | 27.28 | 28.23 | 28.01 | 29.02 | 28.34 | **29.22** |
| 30/18.63 | 24.39 | 25.01 | 24.97 | 25.94 | 25.22 | 26.19 | 26.04 | 27.51 | 26.56 | **28.10** |
| 40/16.13 | 22.55 | 22.67 | 22.57 | 23.76 | 23.19 | 24.76 | 24.66 | 26.35 | 25.11 | **26.78** |

**Table 3**
PSNR values obtained using the proposed denoising method with different priors for two of the test images, *Barbara* and *Peppers*, when $\sigma_\eta = 10$.

| Image | SαS | | Cauchy | | GG | | Laplacian | | Levy | |
|---|---|---|---|---|---|---|---|---|---|---|
| | MAP | MMAE | MAP | MMAE | MAP | MMAE | MAP | MMAE | MAP | MMAE |
| Barbara | 32.97 | 33.62 | 32.13 | 32.71 | 31.98 | 32.48 | 31.51 | 31.83 | 31.46 | 31.75 |
| Peppers | 32.65 | 33.41 | 32.01 | 32.45 | 31.75 | 32.22 | 31.21 | 31.60 | 31.26 | 31.64 |
| | Bi-SαS | | Bi-Cauchy | | Bi-GG | | Bi-Laplacian | | Bi-Levy | |
| | MAP | MMAE | MAP | MMAE | MAP | MMAE | MAP | MMAE | MAP | MMAE |
| Barbara | **34.61** | **34.89** | 33.45 | 33.96 | 33.15 | 33.69 | 32.74 | 33.10 | 33.23 | 33.64 |
| Peppers | **34.29** | **34.59** | 33.13 | 33.61 | 32.68 | 33.18 | 32.24 | 32.53 | 32.87 | 33.29 |

**Table 4**
Averaged PSNR values obtained using the proposed denoising method over 60 textured images [51], when $\sigma_\eta = 20$.

| SαS | | Cauchy | | GG | | Laplacian | |
|---|---|---|---|---|---|---|---|
| MAP | MMAE | MAP | MMAE | MAP | MMAE | MAP | MMAE |
| 28.39 | 29.02 | 28.04 | 28.65 | 28.01 | 28.58 | 27.34 | 28.11 |
| Bi-SαS | | Bi-Cauchy | | Bi-GG | | Bi-Laplacian | |
| MAP | MMAE | MAP | MMAE | MAP | MMAE | MAP | MMAE |
| 29.84 | 30.11 | 29.35 | 29.76 | 29.26 | 29.69 | 28.87 | 29.27 |

for Case 2, the Cauchy PDF, $M = \frac{2y}{\gamma^2+y^2}$, while for Case 3, the Levy PDF, one needs to solve the cubic equation $x^3 + ax^2 + bx + c = 0$, where $a = -y$, $b = \frac{-3\sigma_\eta^2}{2}$ and $c = \frac{\gamma\sigma_\eta^2}{2}$. In the case of the best-fit SαS, we have to numerically compute the Bayesian MAP estimator given by (11).

### 4.2. Bayesian MAP estimator for non-Gaussian noise

We also develop the MAP estimator using zero-mean, independent and identically distributed non-Gaussian noises modelled by the Maxwell and Rayleigh distributions given by

$$P_\eta(\eta) = \begin{cases} \sqrt{\frac{2}{\pi}}\frac{\eta^2}{v^3}\exp\left(\frac{-\eta^2}{2v^2}\right) & \text{Maxwell} \\ \frac{2|\eta|}{\sigma_\eta^2}\exp\left(\frac{-\eta^2}{\sigma_\eta^2}\right) & \text{Rayleigh} \end{cases} \tag{12}$$

where $v = \frac{\sigma_\eta}{\sqrt{3}}$. To obtain the MAP estimate, after inserting the PDFs of the signal and noise into (8), the derivative of the logarithm of the argument in (8) is set to zero resulting in

$$\frac{\partial}{\partial y}\left(\ln(P_\eta(y-x))\right) + \frac{\partial}{\partial y}(-\ln(P_x(y))) = 0 \tag{13}$$

Since for the case of $\alpha=1$, the Cauchy member of the alpha-stable distribution, the PDF has a closed form expression, the Bayesian MAP estimator can be derived, after some manipulations, as a root of the following quartic equation

$$\hat{x}^4 + a\hat{x}^3 + b\hat{x}^2 + c\hat{x} + d = 0 \tag{14}$$

where for the Maxwell noise $a = -2y$, $b = \gamma^2 + y^2$, $c = -2y\gamma^2 - \frac{2y\sigma_\eta^2}{3}$ and $d = \frac{-2\sigma_\eta^2\gamma^2}{3} + \gamma^2y^2$, and for the Rayleigh noise $a = -2y$, $b = \frac{\sigma_\eta^2}{2} + \gamma^2 + y^2$, $c = -2y\gamma^2 - y\sigma_\eta^2$ and $d = \frac{-\sigma_\eta^2\gamma^2}{2} + \gamma^2y^2$. It should be noted that for the general case (best-fit $\alpha$), we obtain the noise-free coefficients numerically.

### 4.3. Bayesian MMAE estimator

We now develop a Bayesian MMAE estimator, using the proposed SαS prior, by minimizing the mean absolute error between the observed data and the estimated one. Since the coefficients in

**Table 5**
PSNR values obtained using the ML method and the proposed parameter estimation method for various noise levels.

| Image | Method | $\sigma_\eta$ | | | | | | | |
|---|---|---|---|---|---|---|---|---|---|
| | | 10 | | 20 | | 30 | | 40 | |
| | | ML | Proposed | ML | Proposed | ML | Proposed | ML | Proposed |
| Barbara | Proposed-MMAE | 34.73 | **34.89** | 31.49 | **31.65** | 28.09 | **28.24** | 26.53 | **26.97** |
| | Proposed-MAP | 34.53 | **34.61** | 31.03 | **31.19** | 27.58 | **27.84** | 26.21 | **26.58** |
| Peppers | Proposed-MMAE | 34.48 | **34.59** | 30.63 | **30.87** | 27.83 | **28.10** | 26.35 | **26.78** |
| | Proposed-MAP | 34.21 | **34.29** | 30.34 | **30.51** | 27.22 | **27.51** | 26.10 | **26.35** |

**Table 6**
PSNR values obtained using denoising methods with various windows and image sizes. (Best result shown in bold.)

| Image | PSNR | | | | | | |
|---|---|---|---|---|---|---|---|
| | $3\times3$ | $5\times5$ | $7\times7$ | $9\times9$ | $11\times11$ | $15\times15$ | $19\times19$ |
| Lena $256\times256$ | 34.61 | **34.82** | 34.75 | 34.64 | 34.49 | 34.22 | 34.01 |
| Lena $512\times512$ | 35.76 | 35.91 | **36.01** | 35.98 | 35.92 | 35.84 | 35.70 |
| Lena $1024\times1024$ | 36.78 | 37.04 | 37.52 | 37.74 | 37.85 | **37.93** | 37.82 |
| Boat $256\times256$ | 32.82 | **32.89** | 32.74 | 32.60 | 32.47 | 32.21 | 32.07 |
| Boat $512\times512$ | 33.65 | 33.87 | **34.05** | 33.93 | 33.81 | 33.56 | 33.40 |
| Boat $1024\times1024$ | 34.24 | 35.20 | 35.62 | 35.80 | 35.89 | **35.96** | 35.82 |
| Peppers $256\times256$ | 33.12 | **33.17** | 33.09 | 32.99 | 32.85 | 32.77 | 32.64 |
| Peppers $512\times512$ | 34.32 | 34.47 | **34.59** | 34.51 | 34.38 | 34.20 | 34.07 |
| Peppers$1024\times1024$ | 35.51 | 35.64 | 35.79 | 35.91 | 36.05 | **36.14** | 36.02 |
| Couple $256\times256$ | 33.00 | **33.06** | 32.95 | 32.87 | 32.73 | 32.61 | 32.49 |
| Couple $512\times512$ | 33.98 | 34.05 | **34.10** | 34.03 | 33.96 | 33.84 | 33.71 |
| Couple $1024\times1024$ | 35.24 | 35.39 | 35.51 | 35.65 | 35.77 | **35.87** | 35.76 |

the approximation subband carry most of the information about the signal to be recovered, we leave them unchanged, and apply the Bayesian MMAE estimator to the coefficients of the detail subbands. The Bayesian MMAE estimator of $x$, given a noisy observation $y$, is given by

$$\hat{x}(y) = \int x P_{x|y}(x|y)dx \tag{15}$$

According to the Bayesian rule, $P_{x|y}(x|y)$ can be written as

$$P_{x|y}(x|y) = \frac{P_x(x)P_{y|x}(y|x)}{\int P_x(x)P_{y|x}(y|x)dx} \tag{16}$$

where $P_x(x)$ is the prior model for the contourlet coefficients of the noise-free image. Substituting (16) into (15), we obtain

$$\hat{x}(y) = \frac{\int x P_x(x)P_{y|x}(y|x)}{\int P_x(x)P_{y|x}(y|x)dx}$$

$$= \frac{\int x P_x(x)P_\eta(\eta)}{\int P_x(x)P_\eta(\eta)dx} \tag{17}$$

where $P_\eta(\eta)$ is the PDF of the noise. In order to estimate the noise-free coefficients, we consider the three cases mentioned above, namely, the Gaussian, Cauchy and the best-fit S$\alpha$S distributions. It should be noted that in the case of the general best-fit S$\alpha$S, the Bayesian MMAE estimator has to be computed by direct numerical integration [48,49]. To lower the computational complexity, we resort to the shrinkage function in terms of a linear convolution as

$$\hat{x}(y) = \frac{P_\eta(y) * xP_x(x)}{P_\eta(y) * P_x(x)} \tag{18}$$

where $*$ is the convolution operator. Therefore, instead of employing direct numerical integration for each coefficient, the Bayesian MMAE estimates of the coefficients of a subband are obtained using the cubic spline interpolation method when the convolution operation is carried out at a limited number of points using the fast Fourier transform (FFT) algorithm as

$$\hat{x}(y) = \frac{F^{-1}\left\{ F\left\{ P_\eta(y)\right\} \cdot F\left\{ xP_x(x)\right\} \right\}}{F^{-1}\left\{ F\left\{ P_\eta(y)\right\} \cdot F\left\{ P_x(x)\right\} \right\}} \tag{19}$$

where $F$ and $F^{-1}$ denote the FFT and inverse FFT transforms, respectively. A consequence of using (19) is reducing the computational effort in obtaining the MMAE estimates.

### 4.4. Parameter estimation

In order to employ the S$\alpha$S prior in denoising, first it is needed to estimate the parameters $\alpha$ and $\gamma$ from the noisy coefficients. There are several estimators, that can be used to estimate the parameters of the alpha-stable distribution, such as the characteristic function-based estimators including regression-type [52] and methods based on minimum distance [53], moments [53], quantiles [48], fractional lower order moments [48,54] and maximum likelihood (ML) [55,56]. Among these, the ML estimator [55] has been shown to provide an efficient estimate of the parameters. We now propose a method for parameter estimation that uses spatially-adaptive fractional lower order moments. We have shown in [40] that when the number of scales is increased, the distribution of the contourlet coefficients is close to the Gaussian distribution. In other words, the distribution of the contourlet coefficients of images is locally Gaussian. In view of this, the dispersion parameter $\gamma$ of an $\alpha$-stable distribution can be estimated as $\gamma = \frac{\sigma^2}{2}$, in which $\sigma^2$ is the variance of the Gaussian distribution in a small spatial window. In order to estimate $\sigma^2$ in a given scale $j$, we employ the spatially-adaptive technique [33] as

$$\hat{\sigma}_j^2(m,n) = \max\left( \sum_{i\in W\left(m-\frac{l-1}{2},n+\frac{l-1}{2}\right)} \frac{y_j^2(i)}{l^2} - \sigma_{\eta,j}^2, 0\right) \tag{20}$$

where $W$ is a square-shaped window of size $l\times l$. The characteristic exponent $\alpha$ is then estimated using the fractional lower order moment (FLOM) method. The moments of order less than $\alpha$ for a S$\alpha$S random variable [48,57,58] are defined as

$$E[|X|^p] = \frac{\gamma^{p/\alpha}\Gamma\left(1-\frac{p}{\alpha}\right)}{\cos\left(\frac{p\pi}{2}\right)\Gamma(1-p)} \tag{21}$$

in which $-1 < p < \alpha \le 2$. It should be noted that the choice of the order $p$ of the fractional moment is arbitrary. However, as shown in [59], the best choice is $p \approx \frac{\alpha}{3}$. In order to estimate the standard deviation of the noise $\sigma_\eta$ from the noisy contourlet coefficients,

**Table 7**
PSNR values obtained using various denoising methods for three of the test images, *Barbara*, *Boat* and *Lena*. (Best results shown in bold and second best in parentheses.)

| | Barbara | | | | Boat | | | | Lena | | | |
|---|---|---|---|---|---|---|---|---|---|---|---|---|
| $\sigma_\eta$ | 10 | 15 | 20 | 25 | 10 | 15 | 20 | 25 | 10 | 15 | 20 | 25 |
| Visu-shrink (hard) [1] | 26.87 | 26.99 | 26.31 | 25.77 | 28.61 | 26.90 | 25.82 | 25.03 | 30.65 | 28.89 | 27.76 | 27.02 |
| SURE-shrink [62] | 30.21 | 28.34 | 27.02 | 25.84 | 31.83 | 29.88 | 28.55 | 27.50 | 33.42 | 31.50 | 30.17 | 29.18 |
| Bayes-shrink [5] | 30.86 | 28.51 | 27.13 | 26.01 | 31.77 | 29.84 | 28.45 | 27.37 | 33.29 | 31.38 | 30.14 | 29.19 |
| HMT [6] | 31.36 | 29.23 | 27.80 | 25.99 | 32.25 | 30.28 | 28.81 | 27.65 | 33.81 | 31.73 | 30.36 | 29.21 |
| LAWMAP [67] | 32.57 | 30.19 | 28.59 | 27.42 | 32.22 | 30.27 | 28.97 | 27.88 | 34.31 | 32.36 | 31.01 | 29.98 |
| Surelet [60] | 32.15 | 29.61 | 27.93 | 26.65 | 32.67 | 30.55 | 29.14 | 28.09 | 34.56 | 32.68 | 31.37 | 30.36 |
| GNW [75] | 32.41 | – | 27.64 | – | – | – | – | – | 33.96 | – | 30.62 | – |
| CW- Bi-shrink [33] | 33.35 | 31.31 | 29.80 | 28.61 | 33.10 | 31.36 | 30.08 | 29.06 | 35.21 | 33.50 | 32.28 | 31.34 |
| LPG-PCA [10] | 32.50 | – | 28.50 | – | – | – | – | – | 33.70 | – | 29.70 | – |
| Trivariate [65] | 33.66 | 31.49 | 29.97 | 28.78 | 33.23 | 31.35 | 30.01 | 28.98 | 35.32 | 33.60 | 32.36 | 31.38 |
| TIDFT [66] | 33.81 | – | 30.37 | – | – | – | – | – | 35.70 | – | 32.98 | – |
| MGGD [61] | – | – | – | – | 33.31 | 31.46 | 30.14 | 29.12 | 35.35 | 33.70 | 32.46 | 31.48 |
| CW-CGSM [63] | 34.01 | 31.79 | 30.25 | 29.07 | 33.49 | 31.51 | 30.13 | 29.09 | 35.50 | 33.72 | 32.40 | 31.35 |
| BLS-GSM [32] | 34.03 | 31.86 | 30.32 | 29.13 | 33.58 | 31.70 | 30.38 | 29.37 | 35.61 | 33.90 | 32.66 | 31.69 |
| NSCT-LAS [64] | 34.09 | – | 30.60 | – | – | – | – | – | 34.46 | – | 32.50 | – |
| K-SVD [11] | 34.42 | 32.37 | 30.83 | 29.60 | 33.64 | 31.73 | 30.38 | 29.37 | 35.61 | 33.90 | 32.66 | 31.69 |
| Fuzzy-shrink [68] | 33.99 | 31.81 | 30.31 | – | 33.67 | 31.75 | 30.24 | – | – | – | – | – |
| WP- shrink [22] | 34.15 | 32.00 | 30.50 | – | 33.52 | 31.70 | 30.38 | – | – | – | – | – |
| NSSTM [69] | 33.56 | – | 30.02 | – | – | – | – | – | 35.87 | – | 32.93 | – |
| EPLL [74] | 33.59 | 31.33 | 29.75 | – | 33.63 | 31.89 | 30.63 | – | 35.56 | 33.85 | 32.60 | – |
| MMSE-MAP [70] | 32.50 | – | 28.55 | – | 32.43 | – | 28.94 | – | 34.29 | – | 31.09 | – |
| NSCCT-NLM [12] | 34.49 | – | 30.99 | – | 33.71 | – | 30.52 | – | 35.98 | – | 32.96 | – |
| NCSR [18] | 34.98 | 33.02 | 31.72 | – | 33.90 | 32.03 | 30.74 | – | 35.81 | 34.09 | 32.92 | – |
| PLOW [20] | – | 32.17 | – | 30.20 | – | 31.53 | – | 29.59 | – | 33.90 | – | 31.92 |
| TDNL [17] | – | – | – | – | – | – | – | – | 35.87 | 34.13 | 32.86 | 31.86 |
| CASD [16] | 34.38 | 32.22 | 30.64 | 29.33 | 33.69 | 31.46 | (30.90) | 29.69 | 34.66 | 32.46 | 30.94 | 29.81 |
| R-NL [13] | – | – | 29.76 | – | – | – | 29.92 | – | – | – | 32.04 | – |
| PID [71] | 34.55 | – | 30.56 | – | 33.77 | – | 29.80 | – | 35.81 | – | 32.12 | – |
| DDID [72] | 34.67 | – | 30.80 | – | 33.74 | – | 29.79 | – | 35.81 | – | 32.14 | – |
| NLB [73] | 34.82 | – | 30.24 | – | 33.91 | – | 29.67 | – | 35.78 | – | 31.80 | – |
| LSSC [15] | 34.97 | 33.00 | 31.57 | 30.47 | (34.02) | **32.20** | 30.89 | 29.87 | 35.83 | 34.15 | 32.90 | 31.87 |
| NHDW [14] | 35.01 | – | (31.79) | (30.70) | – | – | – | – | 35.89 | – | 32.99 | (32.02) |
| BM3D [19] | (34.98) | (33.11) | 31.78 | **30.72** | 33.92 | 32.14 | 30.88 | (29.91) | (35.93) | (34.27) | 33.05 | **32.08** |
| SAIST [21] | **35.23** | **33.32** | **32.10** | – | 33.91 | 32.09 | 30.81 | – | 35.90 | 34.21 | **33.08** | – |
| CT- Bi-SαS-MMAE | 34.89 | 33.02 | 31.65 | 30.57 | **34.05** | (32.19) | **30.95** | **29.94** | **36.01** | **34.34** | (33.06) | 32.01 |

*Donoho*'s estimator [7] is modified in the finest decomposition scale as $\hat{\sigma}_\eta = \frac{1}{0.6745D}\sum_{d=1}^{D}\left(MAD\left\{S_{1,d}\right\}\right)$, where MAD is the *median absolute deviation* and $S_{1,d}$ denotes the $d$th directional subband coefficients in the finest scale.

### 4.5. Proposed denoising algorithm

*Step* 1: Apply the contourlet transform to the noisy image.
*Step* 2: Estimate the parameters $\gamma$, $\alpha$ and $\sigma_\eta$ from the noisy coefficients using the method mentioned in Section 4(c).
*Step* 3: Obtain an estimation of the noise-free coefficients by using the Bayesian MAP (11) or MMAE (17) estimator.
*Step* 4: Apply the inverse contourlet transform to the estimates obtained in Step 3.

The above method of denoising an image is also shown in the form of a block diagram in Fig. 6.

**Table 8**
MSSIM values obtained using proposed denoising method and some of the other existing methods for three of the test images, *Barbara*, *Boat* and *Lena*. (Best results shown in bold and second-best in parentheses.)

| $\sigma_\eta$ | Bayes-shrink | HMT | LAWMAP | CW-Bi-shrink | Trivariate | BLS-GSM | BM3D | CT-Bi-SαS-MMAE |
|---|---|---|---|---|---|---|---|---|
| Barbara | | | | | | | | |
| 10 | 0.92 | 0.93 | 0.93 | 0.94 | 0.94 | 0.95 | **1.00** | (0.96) |
| 20 | 0.85 | 0.87 | 0.87 | 0.88 | 0.89 | 0.91 | **0.98** | (0.94) |
| 30 | 0.78 | 0.79 | 0.81 | 0.83 | 0.82 | 0.84 | **0.95** | (0.91) |
| Boat | | | | | | | | |
| 10 | 0.93 | 0.94 | 0.94 | 0.95 | 0.96 | 0.97 | **1.00** | (0.98) |
| 20 | 0.89 | 0.90 | 0.91 | 0.92 | 0.92 | 0.93 | **0.97** | (0.96) |
| 30 | 0.86 | 0.85 | 0.87 | 0.87 | 0.89 | 0.90 | **0.95** | (0.93) |
| Lena | | | | | | | | |
| 10 | 0.93 | 0.94 | 0.94 | 0.96 | 0.97 | 0.98 | **1.00** | (0.98) |
| 20 | 0.87 | 0.89 | 0.90 | 0.89 | 0.91 | 0.91 | **0.97** | (0.95) |
| 30 | 0.81 | 0.84 | 0.83 | 0.85 | 0.86 | 0.87 | **0.94** | (0.92) |

## 5. Simulation results

The performance of the proposed denoising method is evaluated by conducting experiments using set of images obtained from [50], and then compared to that of the many of the state-of-the-art techniques. The experiments are performed on images corrupted with Gaussian noise of standard deviation, $\sigma_\eta$, varying from 10 to 40. The noisy images are decomposed by the contourlet transform into three scales with eight directions in each scale. Note that any further decomposition beyond these levels does not produce a significant increase in the denoising performance. We use the 9–7 bi-orthogonal filters for both the multi-scale and multi-directional decomposition stages. Since the contourlet transform is not shift-invariant, the denoised image is affected by the pseudo-Gibbs phenomena, resulting in artifacts in smooth regions and ringing effect around the edges. To overcome this problem, as discussed in Section 2, we employ the cycle spinning mode by averaging the result of the contourlet shrinkage method

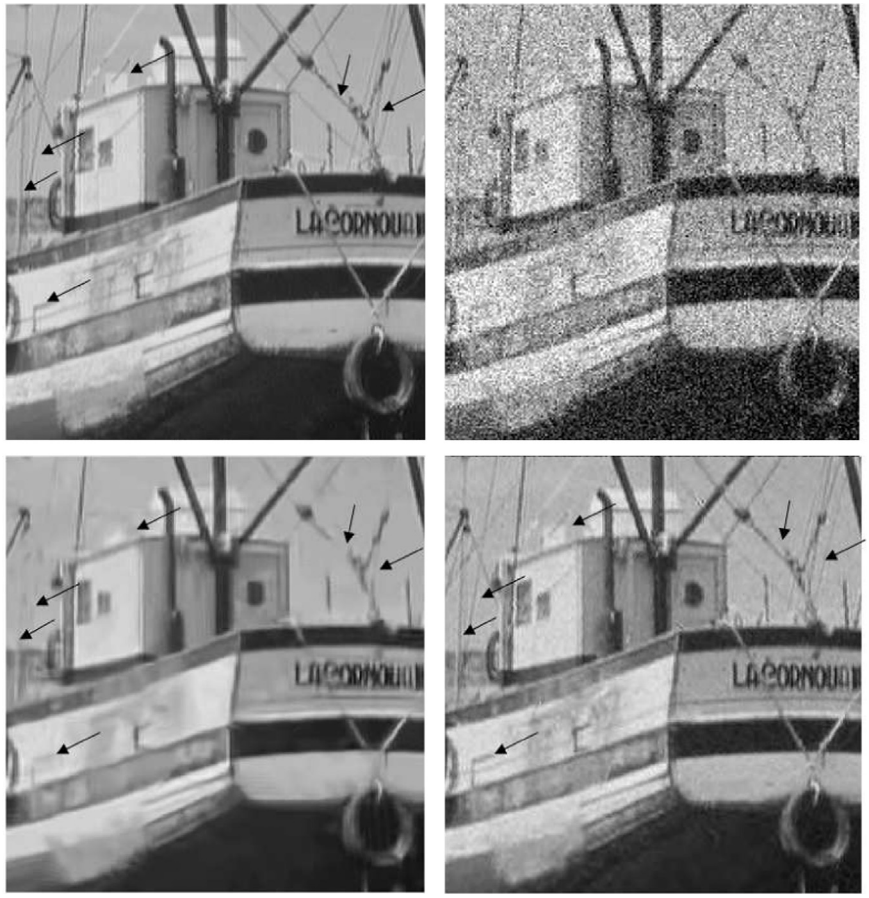

**Fig. 7.** Top-left: original *Boat* image. Top-right: noisy image with $\sigma_\eta = 30$. Bottom-left: denoised using BM3D. Bottom-right: denoised using the proposed method.

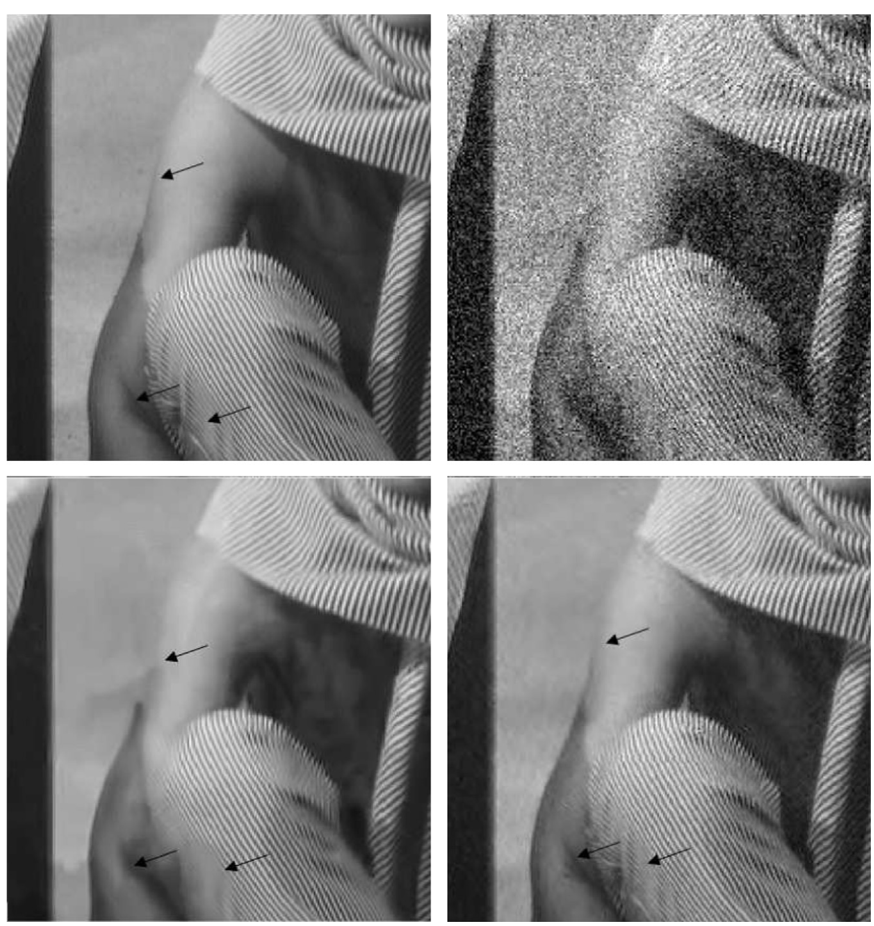

**Fig. 8.** Top-left: original *Barbara* image. Top-right: noisy image with $\sigma_\eta = 30$. Bottom-left: denoised using BM3D. Bottom-right: denoised using the proposed method.

**Fig. 9.** Top-left: original *Lena* image. Top-right: noisy image with $\sigma_\eta = 30$. Bottom-left: denoised using BM3D. Bottom-right: denoised using the proposed method.

**Table 9**
Averaged PSNR values (in dB) obtained using various denoising methods over 1000 images taken from [50]. (Best results shown in bold.)

| Method | Standard deviation | | | |
|---|---|---|---|---|
| | 10 | 15 | 20 | 25 |
| LAWMAP [67] | 33.09 | 31.37 | 29.83 | 28.37 |
| BLS-GSM [32] | 34.53 | 32.78 | 30.97 | 29.76 |
| Trivariate [65] | 34.11 | 32.55 | 30.71 | 29.45 |
| K-SVD [11] | 34.82 | 33.02 | 31.36 | 30.03 |
| BM3D [19] | 35.41 | 33.40 | 32.01 | **30.99** |
| CT-Tri-S$\alpha$S-MMAE | **35.63** | **33.51** | **32.05** | 30.90 |

**Table 10**
Averaged RMSE values obtained for the MAP and MMAE estimators using the alpha-stable family of distributions over a number of test images corrupted by the Maxwell and Rayleigh noises with $\sigma_\eta = 5$. (Best results shown in bold.)

| Noise | Cauchy | | S$\alpha$S | | Bi-Cauchy | | Bi-S$\alpha$S | |
|---|---|---|---|---|---|---|---|---|
| | MAP | MMAE | MAP | MMAE | MAP | MMAE | MAP | MMAE |
| Maxwell | 0.0217 | 0.0195 | 0.0169 | 0.0145 | 0.0164 | 0.0140 | 0.0126 | **0.0102** |
| Rayleigh | 0.0189 | 0.0161 | 0.0147 | 0.0118 | 0.0133 | 0.0112 | 0.0105 | **0.0086** |

over all the circulant shifts of the input noisy image. The peak signal-to-noise ratio (PSNR), in decibels, and the mean structural similarity (MSSIM) index measure are used to provide quantitative evaluations of the algorithm. It should be noted that for a particular noise level, the PSNR value is calculated by repeating the experiment ten times and then averaging over these values. Table 2 gives the PSNR values obtained for various estimators using the alpha-stable family of distributions including the bivariate and univariate S$\alpha$S distributions and its Cauchy member ($\alpha = 1$) in the wavelet and contourlet domains for two of the test images, namely, *Barbara* and *Peppers*. From this table, it is seen that the performance of the denoising algorithm in the contourlet domain is better than that obtained in the wavelet domain, irrespective of the distribution employed. Further, it is observed that the proposed denoising scheme using the bivariate S$\alpha$S distribution provides higher PSNR values than that provided by using the univariate S$\alpha$S. Finally, it is noted that the bivariate alpha-stable distribution in the contourlet domain using the MMAE estimator (CT-Bi-S$\alpha$S-MMAE) provides the highest PSNR values for all the noise levels considered.

We further compare the performance of the S$\alpha$S prior to that of the GG, Cauchy, Levy and Laplacian distributions in our proposed denoising scheme. Table 3 gives the PSNR values obtained using the proposed method when different priors are used for two of the test images, namely, *Barbara* and *Peppers*. It is seen from this table that the bivariate alpha-stable (Bi-S$\alpha$S) distribution provides a better denoising performance than the other distributions do. Similar results are also obtained for other test images, but are not included in view of space limitation. Moreover, to investigate the performance of the proposed denoising scheme on textured images, we apply our proposed denoising algorithm to a set of textured images [51] and the results are given in Table 4. It is seen from this table that the proposed algorithm performs very well even for images with high textures. In order to compare the denoising performance using the proposed parameter estimation method discussed in Section 4.4 with that using the ML method,

**Fig. 10.** (a) *Lena* image corrupted by the Maxwell noise with $\sigma_\eta = 5$, (b) denoised image obtained using BM3D method, RMSE=0.0945, and (c) denoised image obtained using the proposed method, RMSE=0.0883.

**Fig. 11.** (a) *Lena* image corrupted by the Rayleigh noise with $\sigma_\eta = 5$, (b) denoised image obtained using BM3D method, RMSE=0.0051, and (c) denoised image obtained using the proposed method, RMSE=0.0023.

**Table 11**
Averaged SNR values obtained using BM3D [19], Bayesian-CTSD [29] and the proposed denoising schemes over different sets of 512 × 512 EM images. (Best results shown in bold.)

| Exposure time (s)/number of images | $SNR_{in}$ | $SNR_{out}$ | | |
|---|---|---|---|---|
| | | Bayesian-CTSD [29] | BM3D [19] | CT-Bi-S$\alpha$S-MMAE |
| 0.05/20 | 8.54 | 19.25 | 21.32 | **21.35** |
| 0.1/10 | 15.60 | 23.46 | 25.11 | **25.15** |
| 0.2/5 | 22.74 | 30.58 | 31.21 | **31.32** |
| 0.5/2 | 28.90 | 33.85 | 35.47 | **35.58** |
| 1/1 | 33.11 | 36.70 | 37.58 | **37.72** |

the corresponding PSNR values are obtained and presented in Table 5 for various noise levels. It is seen from this table that the proposed method provides higher PSNR values as compared to that provided by the ML method, irrespective of whether a MAP or an MMAE estimator is employed.

The effect of window size on images of various sizes in parameter estimation is now investigated. Table 6 gives the PSNR values obtained using the proposed denoising method for a few of the test images, namely, *Lena*, *Boat*, *Peppers* and *Couple*. It can be seen from this table that the window size of the local variance has an impact on the overall denoising performance. It is observed that, in general, for images of size 1024 × 1024, 512 × 512 and 256 × 256, windows of size of 15 × 15, 7 × 7 and 5 × 5, respectively, give the best denoising results in terms of the PSNR values. Similar results are also observed for other test images.

We now compare the performance of the proposed denoising method, CT-Bi-S$\alpha$S-MMAE, to that of a large number of existing methods, namely, Visu-shrink (hard) [1], Bayes-shrink [5], HMT [6], LPG-PCA [10], K-SVD [11], NSCCT-NLM [12], R-NL [13], NHDW [14], LSSC [15], CASD [16], TDNL [17], NCSR [18], BM3D [19], PLOW [20], SAIST [21], WP-shrink [22], BLS-GSM [32], CW-Bi-shrink [24], Surelet [60], MGGD [61], SURE-shrink [62], CW-CGSM [63], NSCT-LAS [64], Trivariate [65], TIDFT [66], LAWMAP [67], Fuzzy-shrink [68], NSSTM [69], MMSE-MAP [70], PID [71], DDID [72], NLB [73], EPLL [74] and GNW [75]. Table 7 gives the PSNR values obtained using these methods and the proposed method for three of the test images, namely, *Barbara*, *Boat* and *Lena*. It is seen from this table that the proposed CT-Bi-S$\alpha$S-MMAE method provides PSNR values that are generally higher than that provided by the other methods. Table 8 gives MSSIM [76] values obtained using the proposed denoising method and some of the other existing methods for three of the test images, *Barbara*, *Boat* and *Lena*. It is seen from this table that the values of the MSSIM index obtained from our proposed method are generally higher than that of the other methods, except for BM3D in which case our results are comparable, indicating the effectiveness of the proposed method in preserving edges and providing better visual quality.

To subjectively evaluate the performance of the proposed denoising method, the zoomed-in versions of the three test images as well as the denoised versions obtained using the proposed CT-

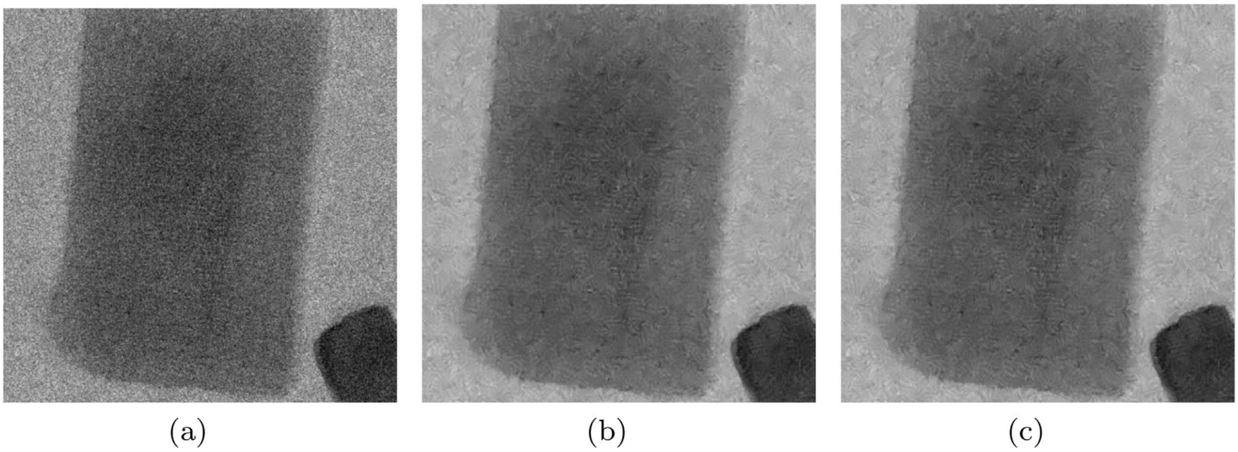

**Fig. 12.** (a) Noisy TM image with exposure time 0.1 s, and the corresponding denoised images using (b) BM3D and (c) proposed method.

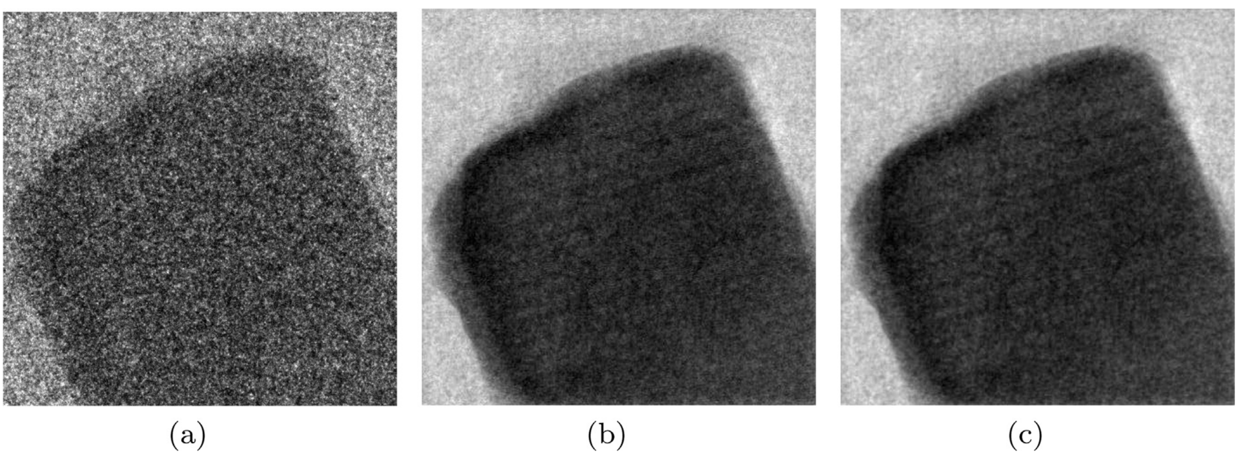

**Fig. 13.** (a) Cropped noisy TM image with exposure time 0.05 s, and the corresponding denoised images using (b) BM3D and (c) proposed method.

**Table 12**
PSNR values obtained using various denoising methods for three of the color images, *Lena*, *Peppers* and *Baboon*. (Best results shown in bold.)

| Method | Standard deviation | | | | |
|---|---|---|---|---|---|
| | 10 | 15 | 20 | 25 | 30 |
| Lena | | | | | |
| Noisy image | 28.13 | 24.61 | 22.13 | 20.17 | 18.60 |
| BLS-GSM [32] | 34.45 | 32.90 | 31.78 | 30.89 | 30.15 |
| Surelet [79] | 34.64 | 33.02 | 31.90 | 31.04 | 30.33 |
| ProbShrink-MB [78] | 34.60 | 33.03 | 31.92 | 31.04 | 29.83 |
| CBM3D [80] | 35.22 | 33.94 | 33.02 | **32.27** | **31.59** |
| CT-Tri-S$\alpha$S-MMAE | **35.25** | **33.95** | **33.05** | 32.21 | 31.43 |
| Peppers | | | | | |
| Noisy image | 28.13 | 24.61 | 22.15 | 20.17 | 18.59 |
| BLS-GSM [32] | 33.26 | 31.89 | 30.92 | 29.46 | 27.47 |
| Surelet [79] | 33.35 | 31.79 | 30.72 | 29.89 | 29.19 |
| ProbShrink-MB [78] | 33.44 | 32.05 | 31.12 | 30.35 | 29.20 |
| CBM3D [80] | 33.78 | 32.60 | 31.83 | **31.20** | **30.61** |
| CT-Tri-S$\alpha$S-MMAE | **33.86** | **32.64** | **31.88** | 31.09 | 30.42 |
| Baboon | | | | | |
| Noisy image | 28.13 | 24.61 | 22.15 | 20.17 | 18.59 |
| BLS-GSM [32] | 30.13 | 27.66 | 26.08 | 24.95 | 24.07 |
| Surelet [79] | 30.49 | 28.15 | 26.64 | 25.55 | 24.71 |
| ProbShrink-MB [78] | 30.15 | 27.72 | 26.17 | 25.04 | 24.16 |
| CBM3D [80] | 30.64 | 28.39 | 26.97 | 25.95 | **25.14** |
| CT-Tri-S$\alpha$S-MMAE | **30.71** | **28.43** | **27.00** | **25.97** | 25.13 |

Bi-S$\alpha$S-MMAE method and the BM3D method when $\sigma_\eta = 30$, are shown in Figs. 7–9. Although the denoised images obtained using BM3D may be visually appealing, a closer look at Figs. 7–9 clearly shows that the denoised images obtained using BM3D are oversmoothened. This oversmoothing diminishes the sharpness of the edges and results in a loss of some details; on the other hand, they are better preserved by the proposed algorithm. This is clearly noticeable, especially from the edges highlighted by the arrows and the surrounding areas.

To further compare the performance of the proposed CT-Bi-S$\alpha$S-MMAE denoising method to that of the other methods. The averaged PSNR values over 1000 images taken from [50] obtained using the proposed denoising scheme and some of the existing image denoising methods are given in Table 9. It is seen from this table that the proposed denoising method provides a better performance in terms of higher PSNR values. It is also observed that the proposed CT-Bi-S$\alpha$S-MMAE denoising method outperforms BM3D, K-SVD, BLS-GSM, Trivariate and LAWMAP methods in 77%, 93%, 96.8%, 98.3% and 100% of the images, respectively. Moreover, to statistically compare the performance of the proposed denoising scheme and that of BM3D, the closest competitor, we compute the $t$-value of confidence [77] between the PSNR sample means of the two methods. The $t$-value of confidence is found to be 1.962, which falls within the 0.05 column of the $t$-table of significance (95%). In view of this, the improvement in the performance of our

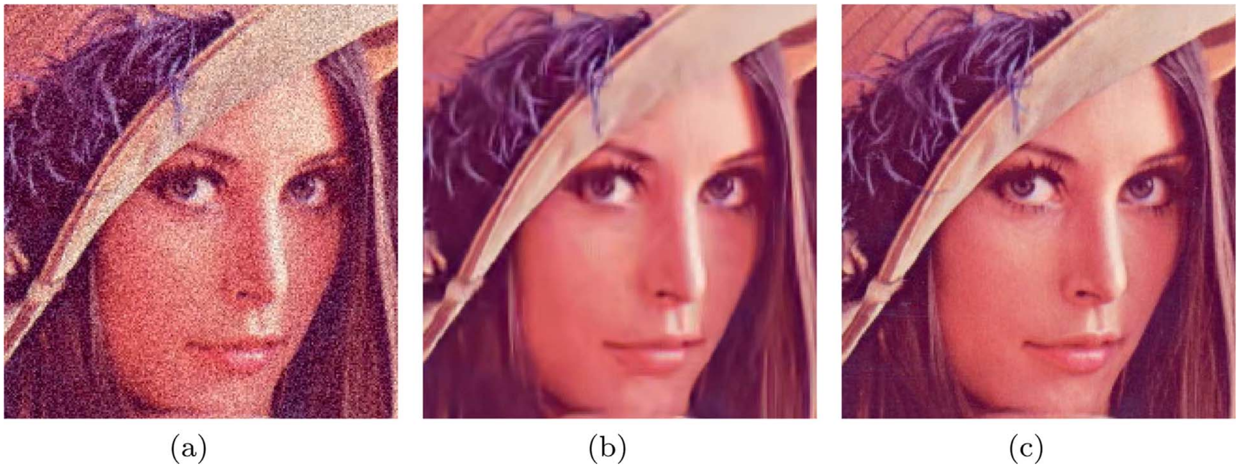

Fig. 14. Color image denoising; (a) cropped noisy *Lena* image with $\sigma_\eta = 20$, PSNR=22.13 dB as well as the corresponding denoised images obtained using (b) CBM3D, PSNR=33.02 dB and (c) the proposed CT-Tri-S$\alpha$S-MMAE, PSNR=33.05 dB.

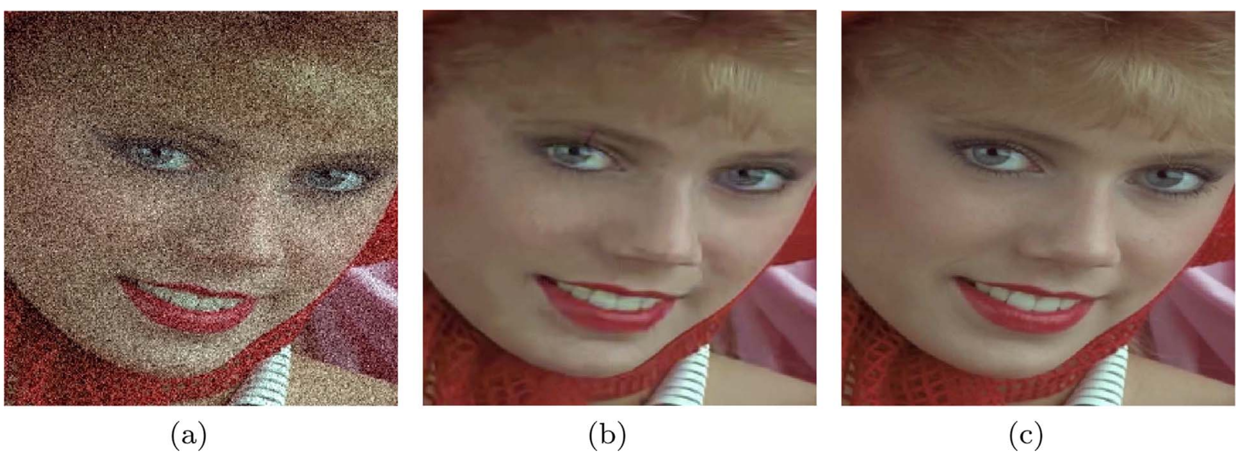

Fig. 15. Color image denoising; (a) cropped noisy *Girl* image with $\sigma_\eta = 30$, PSNR=18.61 dB as well as the corresponding denoised images obtained using (b) CBM3D, PSNR=31.78 dB and (c) the proposed CT-Tri-S$\alpha$S-MMAE, PSNR=31.90 dB.

Fig. 16. Color image denoising; (a) cropped noisy *Peppers* image with $\sigma_\eta = 30$, PSNR=18.59 dB as well as the corresponding denoised images obtained using (b) CBM3D, PSNR=30.61 dB and (c) the proposed CT-Tri-S$\alpha$S-MMAE, PSNR=30.42 dB.

method is significant.

To evaluate the performance of the proposed denoising scheme in the presence of non-Gaussian noises such as Maxwell and Rayleigh, discussed in Section 4.2, we compute the root mean squared error (RMSE) between the original and denoised images. Table 10 gives the averaged RMSE between the original and denoised images obtained for the proposed MAP and MMAE estimators using the alpha-stable family of distributions including the bivariate and univariate S$\alpha$S distributions and its Cauchy member ($\alpha = 1$) over a number of test images. It is seen from this table that the CT-Bi-S$\alpha$S-MMAE gives lower RMSE values indicating its superiority to other estimators in removing non-Gaussian

**Table 13**
Averaged PSNR values obtained using various denoising methods over 24 color images taken from *Kodak* dataset. (Best results shown in bold.)

| Method | Standard deviation | | | | |
|---|---|---|---|---|---|
| | 10 | 15 | 20 | 25 | 30 |
| NLM [12] | 33.45 | 31.49 | 30.06 | 28.93 | 28.00 |
| K-SVD [11] | 34.16 | 32.12 | 30.75 | 29.72 | 28.88 |
| CBM3D [80] | 34.90 | 32.88 | 31.55 | 30.57 | **29.81** |
| CT-Tri-S$\alpha$S-MMAE | **35.01** | **32.95** | **31.61** | **30.59** | 29.80 |

noise. Figs. 10 and 11 illustrate the noisy *Lena* image and the corresponding denoised images obtained using the BM3D and proposed CT-Bi-S$\alpha$S-MMAE denoising methods. It is seen from these figures that the proposed denoising method is superior to BM3D in removing non-Gaussian noise from images. The averaged RMSE over 20 test images obtained using BM3D and the proposed denoising methods are 0.0097 and 0.0086, when images are corrupted by the Rayleigh noise, and 0.0123 and 0.0102, when images are corrupted by the Maxwell noise, respectively. The lower RMSE values obtained using the proposed denoising scheme reinforce its superiority over the BM3D method in removing non-Gaussian noise.

We now investigate the performance of the proposed denoising method on electron microscopy (EM) images. Table 11 gives the averaged signal-to-noise ratios, SNRin and SNRout [29], for the noisy and denoised images, respectively, obtained using the BM3D [19], Bayesian-CTSD [29] and proposed CT-Bi-S$\alpha$S-MMAE methods over the sets of EM images with different exposure times.[1] It is seen from this table that the proposed denoising scheme using the bivariate S$\alpha$S PDF in the contourlet domain is superior to BM3D and the method in [29] in removing noise from the TM images. Figs. 12 and 13 illustrate the noisy TM images with exposure times 0.1 and 0.05 s, respectively, and their corresponding denoised images obtained using the BM3D and proposed denoising schemes. It is seen from these figures that the proposed CT-Bi-S$\alpha$S-MMAE method is better than the BM3D method in removing noise from TM images.

The overall complexity of the proposed CT-Bi-S$\alpha$S-MMAE denoising method is $O\left(\frac{4}{3}l^2N\log N\right)$ for an image of size $N \times N$ and a window of size $l \times l$. More precisely, for denoising an image of size $256 \times 256$, the approximate execution time is 18 s, indicating the computational efficiency of the proposed algorithm.

### *5.1. Color image denoising*

To denoise color images, we consider standard RGB images corrupted by additive Gaussian noise in each channel. The most common approach to denoise color images is to employ the grayscale denoising method for each of the channels. However, in order to take into consideration the dependencies of the RGB channels in color images, we use the trivariate alpha-stable model in the contourlet domain, CT-Tri-S$\alpha$S-MMAE. A comparison with some of the state-of-the-art methods [32,78–80], is given in Table 12 for three of the test images, namely, *Lena*, *Peppers* and *Baboon*. It is seen from this table that the proposed color image denoising method is better than the other methods in terms of the PSNR values, except for the CBM3D method for which our results are comparable. Figs. 14–16 illustrate the cropped noisy *Lena*, *Girl* and *Peppers* images and their corresponding denoised images obtained using the proposed CT-Tri-S$\alpha$S-MMAE and CBM3D methods. It can be seen from this figure that the proposed denoising method is capable of significantly suppressing the noise, preserving the details and providing a better visual quality for denoised images than that provided by CBM3D. To further investigate the performance of the proposed color image denoising, we use another group of test images, namely, the *Kodak* dataset which consists of 24 color images of size $512 \times 768$ [81]. Table 13 gives the averaged PSNR values obtained using the proposed denoising method as well as that yielded by other methods over the *Kodak* dataset. It is seen from this table that the proposed image denoising for color images provides higher PSNR values compared to that yielded by the other methods.

[1] The EM image dataset and the corresponding masks were made available by the authors of [29] to whom we would like to express our thanks.

## 6. Conclusion

In this paper, we have proposed a new image denoising method in the contourlet domain. The proposed method has been carried out by modeling the contourlet subband coefficients of images using the symmetric alpha-stable distribution. The bivariate alpha-stable distribution has been considered to model the across-scale dependencies of the contourlet coefficients. Bayesian MAP and MMAE estimators have been developed by using the proposed prior in order to estimate the noise-free contourlet coefficients. To estimate the parameters of the alpha-stable distribution, a spatially-adaptive method based on fractional lower order moments has been proposed and shown to be superior to the maximum likelihood method. Extensive experiments have been carried out to compare the performance of the proposed denoising method with that provided by the state-of-the-art methods. The results have shown that the proposed denoising method generally outperforms other methods in terms of the PSNR and MSSIM values as well as in terms of the visual quality of the denoised images. These results have been shown to be equally true in the case of color images, where a trivariate alpha-stable distribution has been proposed to capture cross correlations between the RGB color channels.

## Acknowledgements

This work was supported in part by the Natural Sciences and Engineering Research Council (NSERC) of Canada and in part by the Regroupement Strategique en Microelectronique du Quebec (ReSMiQ).

## References

[1] B. Narayanan, R.C. Hardie, E. Balster, Multiframe adaptive Wiener filter super-resolution with JPEG2000-compressed images, EURASIP J. Adv. Signal Process. 55 (1) (2014).
[2] J. Oliveira, J.M. Bioucas-Dias, M.A. Figueire, Adaptive total variation image deblurring: a majorization–minimization approach, EURASIP Signal Process. 89 (2009) 1683–1693.
[3] D.L. Donoho, Denoising by soft thresholding, IEEE Trans. Inf. Theory 41 (3) (1995) 613–627.
[4] E. Bala, A. Ertuzun, A multivariate thresholding technique for image denoising using multiwavelets, EURASIP J. Appl. Signal Process. 8 (2005) 1205–1211.
[5] S.G. Chang, B. Yu, M. Vetterli, Spatially adaptive wavelet thresholding with context modeling for image denoising, IEEE Trans. Image Process. 9 (2000) 1522–1531.
[6] M.S. Crouse, R.D. Nowak, R.G. Baraniuk, Wavelet-based signal processing using hidden Markov models, IEEE Trans. Signal Process. 46 (1998) 886–902.
[7] D.L. Donoho, I.M. Johnstone, Ideal spatial adaptation by wavelet shrinkage, Biometrika 81 (3) (1994) 425–455.
[8] M.N. Do, M. Vetterli, The contourlet transform: an efficient directional multiresolution image representation, IEEE Trans. Image Process. 14 (12) (2005) 2091–2106.
[9] M.N. Do, Directional multiresolution image representations (Ph.D. dissertation), School of Computer and Communication Sciences, Swiss Federal Institute of Technology, 2001.

[10] L. Zhang, W. Dong, D. Zhang, G. Shi, Two-stage image denoising by principal component analysis with local pixel grouping, Pattern Recognit. 43 (4) (2010) 1531–1549.
[11] M. Elad, M. Aharon, Image denoising via sparse and redundant representations over learned dictionaries, IEEE Trans. Image Process. 15 (2006) 3736–3745.
[12] M. Yin, W. Liu, X. Zhao, Q. Guo, R. Bai, Image denoising using trivariate prior model in nonsubsampled dual-tree complex contourlet transform domain and non-local means filter in spatial domain, Optik 124 (2013) 6896–6904.
[13] C. Sutour, Ch.A. Deledalle, J.F. Aujol, Adaptive regularization of the NL-means: application to image and video denoising, IEEE Trans. Image Process. 23 (8) (2014) 3506–3521.
[14] J. Ren, J. Liu, Z. Guo, Nonlocal hierarchical dictionary learning using wavelets for image denoising, IEEE Trans. Image Process. 22 (12) (2013) 4689–4788.
[15] J. Mairal, F. Bach, J. Ponce, G. Sapiro, A. Zisserman, Non-local sparse models for image restoration, in: International Conference on Computer Vision, 2009, pp. 2272–2279.
[16] R. Yan, L. Shao, Y. Liu, Context-aware sparse decomposition for image denoising and super-resolution, IEEE Trans. Image Process. 22 (4) (2013) 1456–1469.
[17] X. Zhang, X. Feng, W. Wang, Two-direction nonlocal model for image denoising, IEEE Trans. Image Process. 22 (1) (2013) 408–412.
[18] W. Dong, L. Zhang, G. Shi, X. Li, Nonlocally centeralized sparse representation for image restoration, IEEE Trans. Image Process. 22 (4) (2013) 1620–1630.
[19] K. Dabov, A. Foi, V. Katkovnik, K. Egiazarian, Image denoising by sparse 3-D transform-domain collaborative filtering, IEEE Trans. Image Process. 16 (8) (2007) 2080–2095.
[20] P. Chatterjee, P. Milanfar, Patch-based near-optimal image denoising, IEEE Trans. Image Process. 21 (4) (2012) 1635–1649.
[21] W. Dong, G. Shi, X. Li, Nonlocal image restoration with bilateral variance estimation: a low-rank approach, IEEE Trans. Image Process. 22 (2) (2013) 700–711.
[22] A. Fathi, A. Naghsh-Nilchi, Efficient image denoising method based on a new adaptive wavelet packet thresholding function, IEEE Trans. Image Process. 21 (9) (2012) 3981–3990.
[23] I.W. Selesnick, R. Baraniuk, N. Kingsbury, The dual-tree complex wavelet transform, IEEE Signal Process. Mag. 22 (6) (2005) 123–156.
[24] J. Yang, Y. Wang, W. Xu, Q. Dai, Image and video denoising using adaptive dual-tree discrete wavelet packets, IEEE Trans. Circuits Syst. Video Technol. 19 (5) (2009) 642–655.
[25] H. Rabbani, M. Vafadust, S. Gazor, I. Selesnick, Image denoising employing a bivariate cauchy distribution with local variance in complex wavelet domain, in: Digital Signal Processing Workshop, 2006, pp. 203–208.
[26] J.L. Starck, E.J. Candes, D.L. Donoho, The curvelet transform for image denoising, IEEE Trans. Image Process. 11 (6) (2002) 670–684.
[27] R. Eslami, H. Radha, The contourlet transform for image denoising using cycle spinning, in: Asilomar Conference on Signals, Systems, and Computers, 2003, pp. 1982–1986.
[28] H. Sadreazami, M. Omair Ahmad, M.N.S. Swamy, Contourlet domain image denoising using the alpha-stable distribution, in: International Midwest Symposium on Circuits and Systems (MWSCAS), 2014, pp. 141–144.
[29] S. Sid Ahmed, Z. Messali, A. Ouahabi, S. Trepout, M. Cedric, S. Marco, Nonparametric denoising method based on contourlet transform with sharp frequency localization: application to electron microscopy images in low exposure time, Entropy 17 (2015) 3461–3478.
[30] A. Achim, E.E. Kuruoglu, Image denoising using bivariate alpha-stable distributions in complex wavelet domain, IEEE Signal Process. Lett. 12 (1) (2005) 17–20.
[31] B. Zhang, J.M. Fadili, J.L. Stark, Wavelets, ridgelets, and curvelets for poisson noise removal, IEEE Trans. Image Process. 17 (7) (2008) 1093–1108.
[32] J. Portilla, V. Strela, M. Wainwright, E.P. Simoncelli, Image denoising using scale mixtures of Gaussians in the wavelet domain, IEEE Trans. Image Process. 11 (2003) 1338–1351.
[33] L. Sendur, I.W. Selesnick, Bivariate shrinkage with local variance estimation, IEEE Signal Process. Lett. 9 (2002) 438–441.
[34] L. Boubchir, J.M. Fadili, A closed-form nonparametric Bayesian estimator in the wavelet domain of images using an approximate alpha-stable prior, Pattern Recognit. Lett. 27 (2006) 1370–1382.
[35] J.M. Fadili, L. Boubchir, Analytical form for a Bayesian wavelet estimator of images using the Bessel K form densities, IEEE Trans. Image Process. 14 (2005) 231–240.
[36] H. Sadreazami, M.O. Ahmad, M.N.S. Swamy, Contourlet domain image denoising using the normal inverse Gaussian distribution, in: Canadian Conference on Electrical and Computer Engineering (CCECE), 2014, pp. 954–957.
[37] H. Sadreazami, M.O. Ahmad, M.N.S. Swamy, Image denoising utilizing the scale-dependency in the contourlet domain, in: International Symposium on Circuits and Systems (ISCAS), 2015, pp. 2149–2152.
[38] L. Sendur, I.W. Selesnick, Bivariate shrinkage functions for wavelet-based denoising exploiting interscale dependency, IEEE Trans. Signal Process. 50 (2002) 2744–2756.
[39] D.D.-Y. Po, M.N. Do, Directional multiscale modeling of images using the contourlet transform, IEEE Trans. Image Process. 15 (6) (2006) 1629–1632.
[40] H. Sadreazami, M.O. Ahmad, M.N.S. Swamy, Contourlet domain image modeling by using the alpha-stable family of distributions, in: International Symposium on Circuits and Systems (ISCAS), 2014, pp. 1288–1291.
[41] H. Sadreazami, M. Omair Ahmad, M.N.S. Swamy, A study of multiplicative watermark detection in the contourlet domain using alpha-stable distributions, IEEE Trans. Image Process. 23 (10) (2014) 4348–4360.
[42] L. Yu, M.N. Do, A new contourlet transform with sharp frequency localization, in: International Conference on Image Processing (ICIP), 2006, pp. 1610–1620.
[43] H. Sadreazami, A. Amini, A robust spread spectrum based image watermarking in ridgelet domain, Int. J. Electron. Commun. 66 (5) (2012) 364–371.
[44] E.J. Candes, D.L. Donoho, Ridgelets: a key to higher-dimensional intermittency?, Philos. Trans. R. Soc. Lond. A 357 (1760) (1999) 2495–2509.
[45] E.J. Candes, D.L. Donoho, Curvelets: a surprisingly effective non-adaptive representation for objects with edges, in: C.R.A. Cohen, L. Schumaker (Eds.), Curve and Surface Fitting, University Press, Nashville, TN, 2000.
[46] E.J. Candes, D.L. Donoho, New tight frames of curvelets and optimal representations of objects with piecewise C2 singularities, Commun. Pure Appl. Math. (2004) 219–266.
[47] R.R. Coifman, D.L. Donoho, Translation-invariant denoising, in: Lecture Notes in Statistics, vol. 103, 1995, pp. 125–150.
[48] C. Nikias, M. Shao, Signal Processing with Alpha-stable Distributions and Applications, Wiley, New York, 1995.
[49] R. Adler, R. Feldman, M. Taqqu, A Guide to Heavy Tails; Statistical Techniques and Applications, Birkhauser, Boston, MA, 1998.
[50] Available online: ⟨http://bows2.ec-lille.fr/⟩.
[51] Available online: ⟨http://sipi.usc.edu/database/⟩.
[52] I. Koutrouvelis, Regression-type estimation of the parameters of stable laws, J. Am. Stat. Assoc. 75 (1980) 918–928.
[53] J. Ilow, Signal processing in alpha-stable noise environments: noise modeling, detection and estimation (Ph.D. thesis), University of Toronto, 1995.
[54] Z. Sun, Ch. Han, Parameter estimation of positive alpha-stable distribution based on negative-order moments, in: International Conference on Acoustics, Speech and Signal processing (ICASSP), 2007, pp. 1409–1412.
[55] J. Nolan, Maximum likelihood estimation and diagnostics for stable distributions (dissertation), Technical Report, Department of Mathematics and Statistics, American University, 1999.
[56] J. Nolan, Information on stable distributions. Available online: ⟨http://academic2.american.edu/~jpnolan/stable/stable.html⟩.
[57] E.E. Kuruoglu, Signal processing in alpha-stable noise environments: a least Lp-norm approach (Ph.D. thesis), University of Cambridge, 1998.
[58] G. Samorodnitsky, M.S. Taqqu, Stable Non-Gaussian Random Processes: Stochastic Models with Infinite Variance, Chapman and Hall, New York, 1994.
[59] G. Tsihrintzis, C.L. Nikias, Fast estimation of the parameters of alpha-stable impulsive interference, IEEE Trans. Signal Process. 44 (6) (1996) 1492–1503.
[60] F. Luisier, T. Blu, M. Unser, A new SURE approach to image denoising: interscale orthonormal wavelet thresholding, IEEE Trans. Image Process. 16 (2007) 593–606.
[61] D. Cho, T.D. Bui, Multivariate statistical approach for image denoising, in: International Conference on Acoustics, Speech and Signal Processing (ICASSP), 2005, pp. 589–592.
[62] D.L. Donoho, I.M. Johnstone, Adaptating to unknown smoothness via wavelet shrinkage, J. Am. Stat. Assoc. 90 (432) (1995) 1200–1224.
[63] Y. Rakvongthai, A. Vo, S. Oraintara, Complex Gaussian scale mixtures of complex wavelet coefficients, IEEE Trans. Signal Process. 58 (7) (2010) 3545–3556.
[64] A.L. DaCunha, Z. Jianping, M.N. Do, The nonsubsampled contourlet transform: theory, design, and applications, IEEE Trans. Image Process. 15 (10) (2006) 3089–3101.
[65] G. Chen, W.-P. Zhu, W. Xie, Wavelet-based image denoising using three scales of dependency, IET Image Process. 6 (6) (2012) 756–760.
[66] Y. Shi, X. Yang, Y. Guo, Translation invariant directional framelet transform combined with Gabor filters for image denoising, IEEE Trans. Image Process. 23 (1) (2014) 44–55.
[67] M.K. Mihcak, I. Kozintsev, K. Ramachandran, P. Moulin, Low-complexity image denoising based on statistical modeling of wavelet coefficients, IEEE Signal Process. Lett. 7 (6) (1999) 300–303.
[68] J. Saeedi, M.H. Moradi, A new wavelet-based fuzzy single and multi-channel image denoising, Image Vis. Comput. 28 (12) (2010) 1611–1623.
[69] G. Gao, Image denoising by non-subsampled shearlet domain multivariate model and its method noise thresholding, Optik 124 (2013) 5756–5760.
[70] H. Om, M. Biswas, MMSE based map estimation for image denoising, Opt. Laser Technol. 57 (2014) 252–264.
[71] C. Knaus, M. Zwicker, Progressive image denoising, IEEE Trans. Image Process. 23 (7) (2014) 3114–3125.
[72] C. Knaus, M. Zwicker, Dual-domain image denoising, in: International Conference on Image Processing (ICIP), 2013, pp. 440–444.
[73] M. Lebrun, A. Buades, J. Morel, A nonlocal Bayesian image denoising algorithm, SIAM J. Imaging Sci. 6 (3) (2013) 1665–1688.
[74] D. Zoran, Y. Weiss, From learning models of natural image patches to whole image restoration, in: International Conference on Computer Vision, 2011, pp. 479–486.
[75] H. Om, M. Biswas, A generalized image denoising method using neighbouring wavelet coefficients, Signal Image Video Process. 9 (1) (2013) 191–200.
[76] W. Zhou, A.C. Bovik, H. Sheikh, E.P. Simoncelli, Image quality assessment: from error visibility to structural similarity, IEEE Trans. Image Process. 13 (4) (2004) 600–612.
[77] S.S. Wilks, Mathematical Statistics, Princeton University Press, New Jersey, 1947.
[78] A. Pizurica, W. Philips, Estimating the probability of the presence of a signal of interest in multiresolution single- and multiband image denosing, IEEE Trans. Image Process. 15 (3) (2006) 645–665.
[79] F. Luisier, T. Blu, SURE-LET multichannel image denoising: interscale orthonormal wavelet thresholding, IEEE Trans. Image Process. 17 (4) (2008)

482–492.
[80] K. Dabov, A. Foi, V. Katkovnik, K. Egiazarian, Color image denoising via sparse 3D collaborative filtering with grouping constraint in luminance–chrominance space, in: International Conference on Image Processing (ICIP), 2007, pp. 313–316.
[81] Available online: ⟨http://r0k.us/graphics/kodak/⟩.